# A DNS STUDY OF TURBULENCE STRUCTURES OF FLOW OF FLUID AT SUPERCRITICAL PRESSURE

**Jundi He**
Department of Mechanical Engineering
University of Sheffield
Sheffield S1 3JD, UK
Email: jhe21@sheffield.ac.uk

**Junjie Yan**
Department of Thermal Engineering
Tsinghua University
Beijing 100084, China
Email: yanjj13@mails.tsinghua.edu.cn

**Wei Wang**
Scientific Computing Department
Science and Technology Facilities Council
Warrington WA4 4AD, UK
Email: Wei.Wang@stfc.ac.uk

**Shuisheng He***
Department of Mechanical Engineering
University of Sheffield
Sheffield S1 3JD, UK
Email: s.he@sheffield.ac.uk
Corresponding author

## ABSTRACT

DNS has been carried out to study the turbulence structures in a uniformly heated vertical pipe with an upward flow of $CO_2$ at supercritical pressure. The flow has been found to undergo a partial and then a full laminarisation followed by recovery. It has been shown that turbulence structures experience reduction then growth during these stages. Small scale structures gradually disappear; the contributions of ejection and sweep events reduce significantly; weak and long streaks are observed when the flow is fully laminarised. The mechanism of turbulence production in the recovery region is different from that of the reference fully developed flow. The body force-aid flow seems to support the new understanding of buoyancy effect developed by He *et al.* (2016).

## INTRODUCTION

There may be various benefits to operate a fluid and/or an energy system at a supercritical pressure, e.g., to increase the thermodynamic efficiency. Examples of such systems include Supercritical Water-cooled Reactor (SCWR) -a type of advanced nuclear reactor and supercritical $CO_2$ power cycles for use to extract geothermal energy or the solar energy, or for coupling with an advanced gas cooled reactor. For fluids at supercritical pressure, significant fluid property variations may take place under strong heating instead of phase change. This makes the flow at supercritical pressure strongly influenced by buoyancy force. The present study investigates the influence of such strong property variations on the turbulence structure and heat transfer behavior, to study the mechanisms behind the general picture.

The effect of buoyancy force is significant in a vertical upward pipe flow of fluids at supercritical pressure with strong heating at the pipe wall due to the big change in density in the near wall region. This may lead to flow laminarisation, causing the well-known heat transfer deterioration. The phenomenon was observed in numerous experiments (Shiralkar & Griffith, 1970; Jackson *et al.*, 2003; Jiang *et al.*, 2006).

Numerical studies on vertical pipe flows with strong heating were also carried out. Reynolds-averaged Navier-Stokes (RANS) simulations have been done for various fluids at supercritical pressure (e.g. He *et al.* (2008); Sharabi *et al.* (2008)). RANS simulation with suitably chose turbulence model can reproduce many experimental observation, through generally speaking RANS can not predict strongly buoyancy-influenced flows reliably. Direct numerical simulations (DNS) was also carried out (Bae *et al.*, 2005; Nemati *et al.*, 2016) for upward and downward pipe flows at different buoyancy conditions. Laminarisation and the regeneration of turbulence at the downstream of the flow can be identified in these DNS studies. Turbulence behaviors under different buoyancy conditions have been studied. Li *et al.* (2008) has conducted DNS of supercritical carbon dioxide in a channel, to study the heat transfer and turbulence characteristics in heating and cooling processes. One of the advantage of numerical studies is that detailed information can be obtained, without the limitation of measurements. This can assist to reveal the mechanism of the interactions between turbulence and heat transfer.

In the present study, the variation of detailed turbulence structures along different stages of the vertical upward pipe flow are shown and investigated to better understand the laminarisation and heat transfer deterioration phenomena of buoyancy-aid flow. The present work will also extend the understanding of the modification of turbulence by non-uniform body forces and flow laminarisation developed by Tuerke & Jiménez (2013), Kühnen *et al.* (2018), Marensi *et al.* (2018) and He *et al.* (2016).

## METHODOLOGY

DNS has been carried out using an in-house code CHAPSim, which is based on the second-order finite differencing discretization of the incompressible flow formulation but with full consideration of temperature dependence fluid properties (Wang & He, 2015). Low Mach number

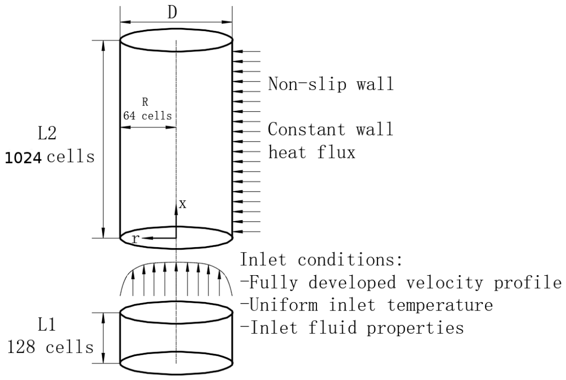


Figure 1. Computational domain and boundary conditions.

approximation (Pierce, 2001) is used in the code. The dimensionless conservative governing equations contain the continuity equation, the momentum equation, and the energy equation are solved:

$$\frac{\partial \rho}{\partial t} + \frac{\partial (\rho U_j)}{\partial x_j} = 0 \tag{1}$$

$$\frac{\partial (\rho U_i)}{\partial t} + \frac{\partial (\rho U_i U_j)}{\partial x_j} = -\frac{\partial p}{\partial x_i} + \frac{1}{Re_0}\frac{\partial \tau_{ij}}{\partial x_j} + \frac{\rho}{Fr} \tag{2}$$

$$\frac{\partial (\rho h)}{\partial t} + \frac{\partial (\rho U_j h)}{\partial x_j} = -\frac{1}{Re_0 Pr_0}\frac{q_j}{x_j} \tag{3}$$

In the above equations, $\rho$ represents the density, $t$ the time, $\tau_{ij}$ the stress tensor, and $p$ the pressure, $U_i$ and $x_i$ are the velocity and spacial coordinates respectively, with the subscript $i$ denoting the directions. $h$ denotes the enthalpy, and $q_i$ the heat flux with the subscript $i$ representing the direction. Superscript * means the values are dimensional. The variables with no superscript are normalized in the following manner(subscript 0 refers to the inlet condition, $R^*$ is the dimensional radius of the pipe):

$$\rho = \frac{\rho^*}{\rho_0^*}, k = \frac{k^*}{k_0^*}, \mu = \frac{\mu^*}{\mu_0^*}, c_p = \frac{c_p^*}{c_{p0}^*}, h = \frac{h^* - h_{ref}^*}{c_{p0}^* T_0^*}, T = \frac{T^*}{T_0^*} \tag{4}$$

$Re$, $Pr$, $Fr$ are the dimensionless groups of Reynolds number, Prandtl number, and Froude number.

$$Re_0 = \frac{\rho_0^* U_0^* R^*}{\mu_0^*}, Pr_0 = \frac{\mu_0^* c_{p0}^*}{k_0^*}, Fr = \frac{U_0^{*2}}{g R^*}, q_j = -\frac{k}{c_p}\frac{\partial h}{\partial x_i} \tag{5}$$

A flow generator is used to produce a fully developed turbulent flow feeding to the inlet of the main pipe section which is heated uniformly (figure 1). The key parameters are as follows: $P^*$=8.67MPa, $\dot{m}$ = $5.235 \times 10^{-4}$kg/s, $T_0^*$=310.15K, $R^*$=0.001m, $L^*$=0.06m, and $q^*$=30870 $W/m^2$. The Reynolds number is 5234. To validate the code CHAPSim under the condition of strong buoyancy-influenced flow and significant property variations, two simulations of vertical upward pipe flow with $CO_2$ at supercritical pressure were carried out and compared with previous studies Bae *et al.* (2005) and Nemati *et al.* (2016). The prediction of the wall temperatures are compared in figure 2. The streamwise distance is normalized by the diameter of the pipe: $x = x^*/D^*$, where $D^*$ is the diameter. The wall temperatures solved by CHAPSim lie between the results obtained in the two other studies, but much closer to the results of Nemati *et al.* (2016). The differences are likely caused by different numerical schemes and fluid properties databases used in the code.

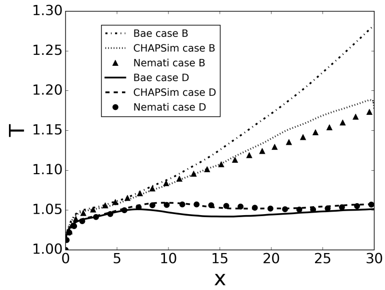


Figure 2. Comparison of streamwise distributions of the wall temperature between different solvers.

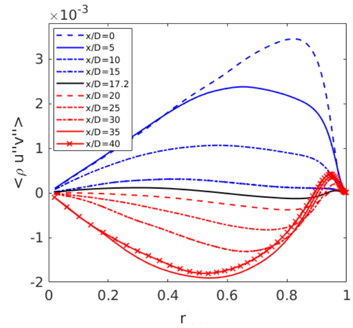


Figure 3. Normalized turbulent shear stress profiles to normalized radius at several chosen streamwise locations.

## RESULT AND DISCUSSION

The results presented in this paper show that the turbulence structure in a heated vertical flow of fluid at supercritical pressure concerned here undergoes significant changes along the length of the pipe. The instantaneous and statistical results are visualized to provide a detailed view of such strongly buoyancy-influenced flow. The statistical results are obtained by time and spacial (only spanwise direction) averaging. Considering the strong variation of density, Favre average, instead of time average is used:

$$\tilde{\phi} = \frac{\langle \rho \phi \rangle}{\langle \rho \rangle} \tag{6}$$

The tilde "$\sim$" and the angle bracket "$\langle\rangle$" denote the Favre and time averaged values respectively. The fluctuation of time average denotes by prime: $u' = U - \langle U \rangle$, that of the Favre average denotes by double prime: $u'' = U - \tilde{U}$.

The Favre averaged turbulence shear stress and axial velocity profiles in several streamwise locations are shown

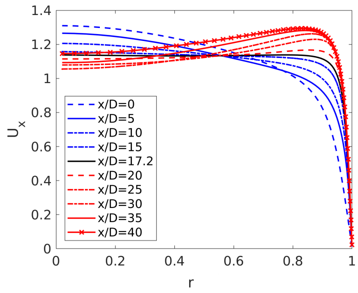


Figure 4. Normalized axial velocity to normalized radius at several chosen streamwise locations.

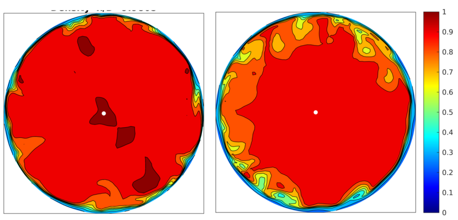

Figure 5. Contours of normalized density $\rho$ at x=10 and 30.

in figures 3 and 4. "r" is the normalized radius: $r = r^*/R^*$, where $R^*$ is the radius of the pipe. From the variation of the turbulence shear stress $\langle \rho u'' v'' \rangle$, the flow can be conveniently divided into several regions: (i) the reference flow (Region 1: x/D$\approx$ 0); (ii) Partial laminarisation (Region 2: $5 < x < 17$): Soon after the start of the heating the turbulence activities reduce with distance; (iii) Full laminarisation (Region 3: $17 < x < 20$): the turbulence shear stress is close to zero but the normal stresses are not necessarily zero (see later) and (iiv) Recovery (Region 4, $x > 20$): finally turbulence is reproduced. The turbulent shear stress takes the shape and values of a "standard" shear flow at the inlet to the heated region. When the flow is under strong heating, the temperature of the near wall region reaches the critical temperature, with a significant reduction of density, causing strong buoyancy. Figure 5 shows the contours of normalized density at x =10 and 30. They are at the partial laminarisation and recovery region, respectively. At x=10, the normalized density at most part of the region in the core is nearly 1, while some spots of low density appear near the wall. At x=30, these spots gradually grow into the main stream, occupying a larger space in the near wall region. This density pattern corresponds to the "M-shape" velocity profile in figure 4. It explains the strong local acceleration near the wall, causing the flip of the velocity profile to a "M-shape" profile at the later stage.

The streamwise variations of the buoyancy parameter $Bo^*$, Reynolds number $Re$, and Nusselt number $Nu$ are shown in figure 6. The Nusselt number decreases rapidly after the entrance of the heating section due to the development of the thermal boundary layer and the reduction of turbulence. After a certain distance, the reduction rate is smaller, and the main reason for the heat transfer deterioration here is the reduction of turbulence. At about x=19, the Nusselt number reaches the minimum value, after which it start increasing, corresponding to the regeneration of the turbulence at the recovery stage. From about x=32, the Nusselt number remains largely constant, eventhough Re continue increasing. For comparison, the empirical correlation

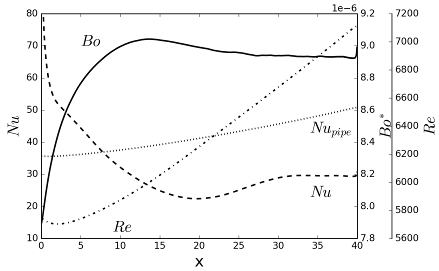


Figure 6. Streamwise variations of buoyancy parameter, Reynolds number, and Nusselt number.

of Dittus-Boelter for forced convection

$$Nu_{pipe} = 0.023 \times Re^{0.8} Pr^{0.4} \tag{7}$$

is also plotted in figure 6. The local Nusselt number is lower than that of forced convection with the same $Re$ and $Pr$ number in most part of the pipe including in the recovery region. This can be explained by figure 3, at about x=35, the turbulence shear stress recovers significantly in comparison with that in the full laminarisation region. In most part, the magnitude of the turbulence shear stress at the recovery stage is still lower than that at the entrance of the pipe, which represents a typical fully developed turbulent flow. As a result, the turbulence thermal diffusivity at the recovery stage is still lower than that in forced convection.

The Reynolds number in figure 6 is calculated using the bulk fluid properties and axial velocity. The streamwise growth of Reynolds number suggests the laminarisation is not related to the variation of the Reynolds number. To visualize the strength of the buoyancy, the buoyancy parameter (Jackson, 1979) is used, which is calculated using the Grashof number based on heat flux:

$$Bo = \frac{Gr}{Re^{3.425} \times Pr^{0.8}}, \quad \text{where} \quad Gr = \frac{g^* \beta^* D^{*4} q^*}{\lambda \nu^2}. \tag{8}$$

The axial variation of the buoyancy parameter is plotted in figure 6. The buoyancy parameter increases rapidly after the entrance, reaches the maximum at about x=14. The buoyancy parameter is much larger than the criterion of significant buoyancy force, which is $5.6 \times 10^{-7}$.

In figure 7 (a), the contour of the normalized fluctuating streamwise velocity of a wall-parallel plane at $y^{+0} = 2.21$ is shown, and in figure 7 (b), the iso-surfaces of $\lambda_2 = -0.4$ are shown, colored by the distance from the wall. $\lambda_2$ is the second largest eigenvalue of the symmetric tensor $S^2 + \Omega^2$ ($S$ and $\Omega$ are the symmetric and antisymmetric parts of the velocity gradient tensor $\nabla u^*$). The overall response of the turbulence can be visualized from figure 7, which is separated into 4 regions axially, with red text labels specifying the name of the corresponding region. Superscript "0" of $y^{+0}$ denotes that the fluid properties used to calculate the $y^+$ values are properties at the inlet of the heating section. In figure 7, turbulence activities gradually reduce in the partial laminarisation region. The streaks of axial velocity fluctuation $u'$ are elongated, and the vortexes in the core of the flow disappear. Longer and weak streaks appear in fully laminarisation region, corresponding to the streamwise location where the turbulence shear stress $\langle \rho u'' v'' \rangle$ are nearly zero at most radial locations (figure 3, x=17.2). After

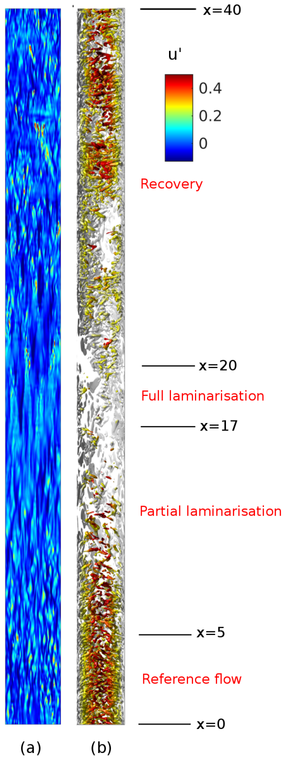


Figure 7. (a) Contour of normalized streamwise fluctuating velocity at a wall-parallel plane at $y^{+0} = 2.21$, (b) isosurfaces of $\lambda_2 = -0.4$, colored by distance to the wall (red: main stream, yellow: middle region, grey: near wall region)

about x=20, turbulence activities grow again, and vortexes are firstly regenerated near the wall. Then at about x=28, vortexes appear in the core flow region, weaker but similar to the pattern at the entrance, suggesting the turbulence is regenerated, and heat transfer is enhanced again. The same phenomena can also be observed in figure 7 (a). Strong fluctuations (deep red) are presented at the entrance; then all disappear in the partial laminarisation and full laminarisation region.

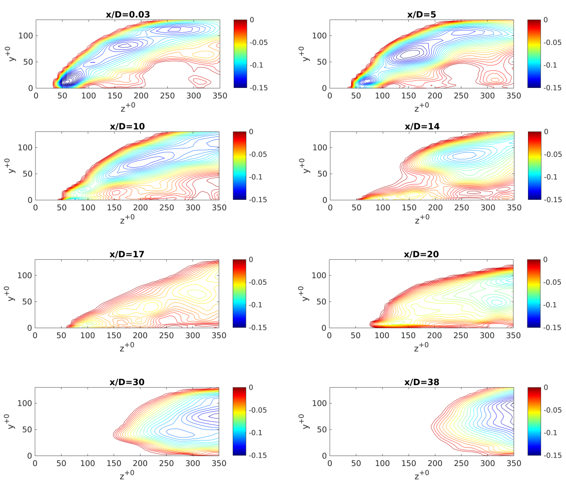


Figure 8. Time averaged panwise correlation of the streamwise velocity (positive values removed).

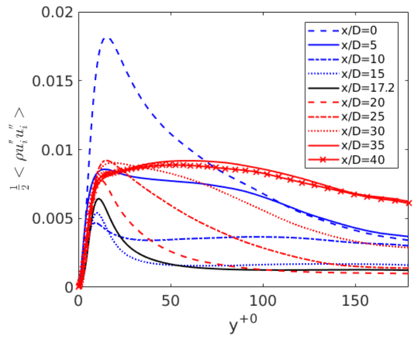


Figure 9. Streamwise development of turbulent kinetic energy ($\frac{1}{2}\langle\rho u_i'' u_i''\rangle$) profiles.

Figure 8 shows the time averaged spanwise correlations for the streamwise velocity in several streamwise locations, with positive values removed. The variation of streak structures along the pipe can be visualized. At the entrance (x=0.03), relatively strong negative correlation can be observed at $y^{+0} = 15$ and $z^{+0} = 70$, indicating that the spanwise spacing of the near wall streaks are about $\Delta z^{+0} = 140$. Two weaker negative correlations can be seen further from the wall, with spanwise spacing of $\Delta z^{+0} = 340$ and 530. After a short distance of heating, at x=5, the near wall streaks become weaker, but the one with larger size and further from the wall becomes stronger compared with itself at the entrance. At x=10, the streaks near the wall is weaker than the larger one, which is at about $y^{+0} = 125$. The flow is partial laminarised at this stage. At x=14, right before the fully laminarisation region, the near wall negative correlation gradually disappears, and the larger one is also weaker. The weakest correlations appear at x=17, corresponding to the begin of the full laminarisation stage. At the beginning of the recovery region (x=20), turbulence activities grow again, with relatively strong negative correlation spots appear at $y^{+0} = 50 \sim 100$. The large but weak negative correlations merge into one in the recovery stage, which is very different from the pattern of the reference fully developed flow at the entrance.

The turbulence structure evolutions observed in figure 7 & 8 are reflected in the streamwise development of the turbulent kinetic energy profiles, which is shown in figure 9. Near the entrance (x=0), k peaks at about $y^{+0} = 15$, corresponding to the strong negative correlation near the wall. The peak value reduces progressively under the effect of the body force. After x=5, the turbulent kinetic energy in the core flow ($y^{+0} > 100$) is also decreasing. Until x=10, there appears to be 2 peaks in the profile, with one in the near wall region and another one in the core flow. After about x=10, the turbulence kinetic energy in the core flow still decreases, but that of the near wall region starts to grow, and this is before the flow reaching the full laminarisation region. From x=10 to 17.2, turbulent kinetic energy in most part of the pipe reduces, but the peak near the wall increases. After the fully laminarisation region, turbulence begins to be regenerated, and the growth of the turbulence kinetic energy is mainly in the region with $y^{+0} > 15$. After x=35, the peak value is moved further from the wall, at about $y^{+0} = 60$, which seems to correspond to the centre of negative correlation in figure 8 at the same location. At the end of the recovery region, turbulence is more uniform in the radial direction, different from the profile of the reference turbulence flow. The profiles of the production

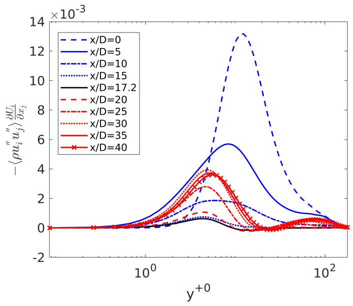


Figure 10. Radial distributions of production of turbulent kinetic energy ($-\langle\rho u_i^{''} u_j^{''}\rangle \frac{\partial U_i}{\partial x_j}$) at several streamwise locations in semi-log plot.

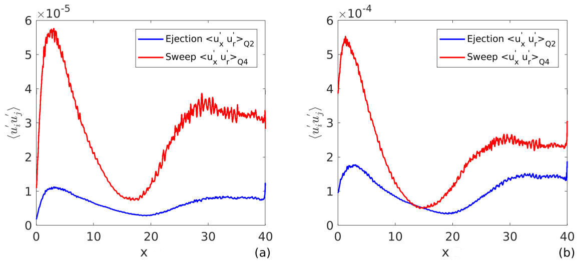


Figure 11. Contributions of ejection (Q2) and sweep (Q4) event at (a) $y^{+0} = 1.4$, (b) $y^{+0} = 5.6$.

of the turbulent kinetic energy in these chosen streamwise locations are plotted in figure 10 in a semi-log manner to view the near wall behavior clearly. From x=0 to 17.2, the peak value of the profile decreases rapidly, and the peak location is gradually moving toward the wall. At x=17.2, the flow is fully laminarised. In the recovery region, the shear production gradually increases again, with the peak locating close to the wall, and there is another smaller peak in the core flow. The near wall peak is mainly caused by the largest $\frac{\partial U}{\partial y}$, but the magnitude of the turbulent shear stress $\langle\rho u^{''} v^{''}\rangle$ at this location is relatively low, thus the peak value at this location is lower than that of the reference flow. The peak at about $y^{+0} = 90$ is caused by the maximum absolute turbulent shear stress, the peak of which moves toward the core flow during the recovery stage. Due to the smaller $\frac{\partial U}{\partial y}$ in the core flow, the peak production here is lower than the one near wall.

To quantify the contribution of ejection and sweep events at near wall region, the hyperbolic hole introduced by Lu & Willmarth (1973) is used here, with the contribution of the corresponding turbulent event denoted by:

$$\langle u_x^{'} u_r^{'}\rangle_Q = \lim_{T\to\infty} \frac{1}{T}\int_0^T \langle u_x^{'} u_r^{'}\rangle I(t)dt, \tag{9}$$

in which "Q" represents the quadrant corresponding to of ejection ($u_x^{'} < 0$, $u_r^{'} < 0$) and sweep ($u_x^{'} > 0$, $u_r^{'} > 0$), T denotes the cell number in spanwise direction, $I(t)$ is a pointer to specify if the local cell is counted in such event:

$$I(t) = \begin{cases} 1, & \text{if } \mid u_x^{'} u_r^{'} \mid \geq h \times u_{x,rms}^{'} u_{r,rms}^{'} \\ 0, & \text{if } \mid u_x^{'} u_r^{'} \mid < h \times u_{x,rms}^{'} u_{r,rms}^{'} \end{cases}. \tag{10}$$

$h$ is a parameter to filter the weak event. With larger h, the stronger event can be obtained. $h = 1$ is used in the current quadrant analysis, the contributions of the ejection and sweep event at two near wall locations ($y^{+0} = 1.4$ & $5.6$) are shown in figure 11. Initially, sweep dominate the flow. The contributions of ejection and sweep reduces rapidly when the flow is being laminarised, suggesting the effect of body force weakens the two events, and they both reach the minimum around the fully laminarised stage. The contributions of sweep event reach the minimum faster than that of the ejection at both the two locations. When the flow is fully laminarised, the two events are nearly equilibrium. During the recovery stage, the contributions of the two event grow together, and remain at certain level after about x=30. At $y^{+0} = 1.4$, the magnitude of the contributions is lower compared to that at $y^{+0} = 5.6$, but the contribution of sweep is about 3 times higher than that of the ejection, while at $y^{+0} = 5.6$, this difference is smaller.

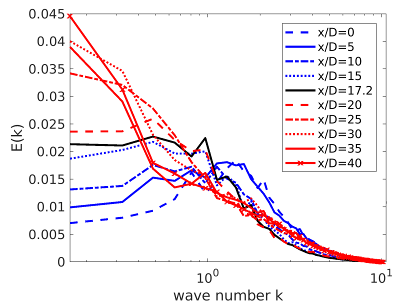


Figure 12. Development of spanwise wavenumber spectrum at $y^{+0} = 4.48$ in semi-log plot.

The development of the energy spectrum at a wall locations ($y^{+0} = 4.48$) is shown in figure 11. Significant streamwise growth in large scale range can be seen during the laminarising and recovery stage. This phenomenon agrees with the trend observed in the correlations. However, the energy in the inertial range gradually reduces. Laminarisation lowers the frequency of the flow (more energy is located in large scale, low frequency eddies), but appears to helps to form large scale structures located further from the wall. In this process, the near wall short and strong streaks are weakened and elongated, and turbulent events are restrained.

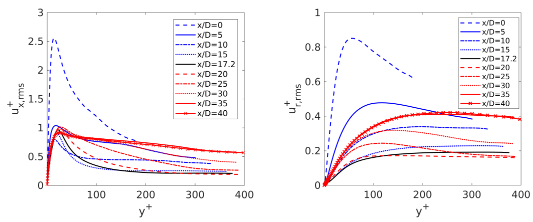


Figure 13. Root mean square of streamwise and radial fluctuating velocity normalized by $u_\tau$ at several streamwise locations.

Figure 13 shows the profiles of root mean square of the fluctuating streamwise and radial velocity $u_{x,rms}^{+}$ and $u_{r,rms}^{+}$, normalized by $u_\tau$ based on the local properties. At x=17.2, although the turbulence shear stress $\langle\rho u_x^{''} u_r^{''}\rangle$ is close to zero in most of the region, $u^+_{x,rms}$ and $u^+_{r,rms}$ still remain certain value ($u^+_{x,rms} \sim 0.25$ and $u^+_{r,rms} \sim 0.2$ for $y^+ > 100$). It suggests that the two fluctuation components are not correlated when the flow is fully laminarised. At the partial laminarised stage, the two components gradually reduce. Under the influence of body force, the two fluctuating components behave differently at different stages. According to the new understanding of the buoyancy-aid flow provided in He *et al.* (2016), the buoyancy-influenced flow can be seen to be a combination of an equal pressure gradient (EPG) flow and the additional perturbation flow due to the buoyancy force. Such understanding was developed for a fully developed flow with constant radial distribution of buoyancy force. In He *et al.* (2016), the apparent friction velocity $u_{\tau 1} = (\frac{D}{4\rho}\frac{dP}{dx})^{0.5}$ was used to calculate the fluctuating velocity $u^{+1}_{i,rms}$ and the dimensionless distance $y^{+1}$, to remove the contribution of buoyancy force to the wall shear stress. Figure 14 shows the profiles of $u^{+1}_{x,rms}$ and $u^{+1}_{r,rms}$ in several streamwise locations before the flow is fully laminarised. After removing the contribution of the buoyancy force, the profiles agrees well at the near wall region at which the buoyancy is relatively strong. In this scenario, the reduction of the apparent Reynolds number is responsible for the drop of $u^{+1}_x$ and $u^{+1}_r$.

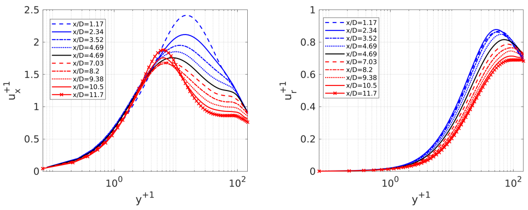


Figure 14. Root mean square of streamwise and radial fluctuating velocity normalized by $u_{\tau 1}$ at several streamwise locations.

## CONCLUSIONS

In the present study, the vertical upward pipe flow of carbon dioxide at supercritical pressure is simulated using DNS. The flow is heated and the fluid temperature reaches the critical temperature near wall, and the flow is subjected to strong buoyancy-influence. The development of the flow can be divided into four regions and the turbulence structures in these regions are studied. A better understanding of the mechanism has been gained. During the process of laminarisation, near wall streaks are elongated and weakened, instability reduces, and turbulence events become sparse. In the recovery region, turbulence is regenerated, but turbulence structures are mostly of large scales, and the radial distribution of the turbulent kinetic energy is more uniform compared to the typical fully developed turbulent flow. The result agrees well with the new understanding developed by He *et al.* (2016), after removing the contribution of buoyancy. The effect of buoyancy force can be estimated by a additional perturbation flow.

## REFERENCES

Bae, Joong Hun, Yoo, Jung Yul & Choi, Haecheon 2005 Direct numerical simulation of turbulent supercritical flows with heat transfer. *Physics of Fluids* **17** (10).

He, S., He, K. & Seddighi, M. 2016 Laminarisation of flow at low Reynolds number due to streamwise body force. *Journal of Fluid Mechanics* **809**, 31–71.

He, S., Kim, W. S. & Bae, J. H. 2008 Assessment of performance of turbulence models in predicting supercritical pressure heat transfer in a vertical tube. *International Journal of Heat and Mass Transfer* **51** (19-20), 4659–4675.

Jackson, J.D. 1979 Influences of buoyancy on heat transfer to fluids flowing in vertical tubes under turbulent conditions. *Turbulent forced convection in channels and bundles 2* pp. 613–640.

Jackson, J.D., Lutterodt, K.O.J. & Weinberg, R. 2003 Experimental Studies of Buoyancy-influenced Convective Heat Transfer in Heated Vertical Tubes at Pressures Just Above and Just Below the Thermodynamic Critical Value. In *In Proceedings of the Joint International Conference on Global Environment and Nuclear Energy System/Advanced Power Plants*, pp. 15–19.

Jiang, Pei Xue, Shi, Run Fu, Xu, Yi Jun, He, S. & Jackson, J. D. 2006 Experimental investigation of flow resistance and convection heat transfer of CO2 at supercritical pressures in a vertical porous tube. *Journal of Supercritical Fluids* **38** (3), 339–346.

Kühnen, Jakob, Song, Baofang, Scarselli, Davide, Budanur, Nazmi Burak, Riedl, Michael, Willis, Ashley P., Avila, Marc & Hof, Björn 2018 Destabilizing turbulence in pipe flow. *Nature Physics* **14** (4), 386–390.

Li, Xinliang, Hashimoto, Katsumi, Tominaga, Yasuhiro, Tanahashi, Mamoru & Miyauchi, Toshio 2008 Numerical Study of Heat Transfer Mechanism in Turbulent Supercritical CO2 Channel Flow. *Journal of Thermal Science and Technology* **3** (1), 112–123.

Lu, S. S. & Willmarth, W. W. 1973 *Measurements of the structure of the Reynolds stress in a turbulent boundary layer*, , vol. 60.

Marensi, Elena, Willis, Ashley P & Kerswell, Rich R 2018 Stabilisation and drag reduction of pipe flows by flattening the base profile. *arXiv preprint, arXiv:1806.05693*.
.

Nemati, Hassan, Patel, Ashish, Boersma, Bendiks J. & Pecnik, Rene 2016 The effect of thermal boundary conditions on forced convection heat transfer to fluids at supercritical pressure. *Journal of Fluid Mechanics* **800**, 531–556.

Pierce, Charles David 2001 Progress-Variable Approach for Large-Eddy. PhD thesis.

Sharabi, M., Ambrosini, W., He, S. & Jackson, J. D. 2008 Prediction of turbulent convective heat transfer to a fluid at supercritical pressure in square and triangular channels. *Annals of Nuclear Energy* **35** (6), 993–1005.

Shiralkar, B. & Griffith, P. 1970 The Effect of Swirl, Inlet Conditions, Flow Direction, and Tube Diameter on the Heat Transfer to Fluids at Supercritical Pressure. *Journal of Heat Transfer* **92** (3), 465.

Tuerke, Florian & Jiménez, Javier 2013 Simulations of turbulent channels with prescribed velocity profiles. *Journal of Fluid Mechanics* **723**, 587–603.

Wang, Wei & He, Shuisheng 2015 Mechanisms of buoyancy effect on heat transfer in horizontal channel flow. In *The 7th International Symposium on Supercritical Water-Cooled Reactors (ISSCWR-7)*, pp. 15–18.